

# Single Molecule Studies Under Constant Force Using Model Based Robust Control Design

Shreyas Bhaban\*, *Student Member, IEEE*, Saurav Talukdar\*, *Student Member, IEEE*, Subhrajit Roychowdhury, Mingang Li, Thomas Hays, and Murti Salapaka, *Member, IEEE*

**Abstract**—Optical tweezers have enabled important insights into intracellular transport through the investigation of processive motor proteins, owing to the ability to manipulate particles at the nanoscale with force resolution in femto newtons. The investigations have led to substantial understanding of motor protein functionality and how malfunctions in motor proteins disrupts transport inside the cells, being the likely cause of several neurodegenerative diseases and muscular disorders. These studies typically utilize spherical cargoes as handles to probe the motor motion. The motor proteins operate under varying load forces, necessitating studies under controlled forces to understand their response to different loading conditions. It is achieved through feedback control designs, that regulate the load force on the cargo to the desired value in the presence of disturbances (primarily, motor motion). The varying nature of the unmeasured disturbances and the effect of thermal noise pose key challenges for efficient force regulation. Furthermore, an accurate estimation of motor motion is necessary to provide important statistics regarding the motor stepping, detachment and reattachment behavior. It is achievable through the utilization of linear Hookean springs to model the motors and infer its motion from measured position of the optical cargo and is facilitated by force clamping mechanisms with high bandwidths of disturbance rejection. Existing methodologies lack the required model-based designs and precise guarantees on closed loop performances. Moreover, heavy corruption of measured cargo data with thermal noise prevents direct estimation of motor stepping statistics, necessitating current techniques of motor motion estimation that use offline algorithms. In this article, we propose a mixed objective  $H_2/H_\infty$  optimization framework using a model-based design, that achieves the dual goals of force regulation and real time motion estimation with quantifiable guarantees. Here, we minimize the  $H_\infty$  norm for the force regulation and error in step estimation while maintaining the  $H_2$  norm of the noise on step estimate within user specific bounds. We demonstrate the efficacy of the framework through extensive simulations and an experimental implementation using an optical tweezer setup with live samples of the motor protein ‘kinesin’; where regulation of forces below 1 pN with errors below 10% is obtained while providing real time estimates of motor motion. The design further enables the investigation of motor proteins at their native speeds, circumventing the current need to reduce motor

speeds to allow for their investigation using existing techniques.

**Keywords**—Optical trapping, Optical force clamp, Intracellular Transport, Molecular motor proteins, System Identification, Acousto-Optic Deflector (AOD), Mixed objective  $H_2/H_\infty$  optimization, Kinesin motility assay.

## I. INTRODUCTION

Transport of important cargo inside the cells of eucaryotic species occurs through molecular motor proteins such as kinesin, dynein and myosin. These motor proteins enable directed transport of cargo by converting chemical energy to kinetic energy and are central to the regulatory mechanisms that maintain the internal organisation of the cell [1], [2]. Structurally, the motor proteins are composed of a cargo binding tail domain, a stalk and two motor heads; where the motor heads bind to the microtubule filaments while transporting the cargo as shown in Fig. 1. The tail domain attaches to the cargo of interest while the motor heads take discrete steps (or ‘walk’) over the pathways inside the cell (composed of microtubules) [3], thereby enabling directed transport of cargo. The typical motion of a single motor protein constitutes of series of discrete stepping events [4]. The motor proteins are responsible for numerous intracellular functions, ranging from producing muscle contraction and cellular tension to transport of sub-cellular commodities inside the cytoplasm; hence, proper functioning of molecular motors is necessary to maintain a healthy cellular environment. Disruption of the transport mechanism due to impaired motor protein behavior is known to cause a host of maladies, including neurodegenerative diseases such as Huntington’s, Parkinsons and Alzheimers Disease [5], [6], high blood pressure and muscular disorders such as heart disease. Thus, the study of motor proteins is important to comprehend the intracellular functionality.

Challenges in investigation of motor motion through direct observation (using confocal or transmission electron microscopy) stem from the extremely small dimensions and step sizes of the motor proteins. For example, kinesin is about 110 nm in length and takes 8 nm sized steps, while exerting forces in the range of femto newtons on the cargo. An efficient method of probing molecular motors is through the use of optical traps [9], [10], which use a highly focused laser beam to trap micron-sized dielectric beads suspended in a suitable liquid medium, as shown in Fig. 2. When the beam is passed through a high numerical aperture (NA) objective, the interaction of the bead with the reflected and refracted rays of the laser, results in formation of a stable equilibrium point near the focus of the objective [11]. For small values of bead

\*Both authors have contributed equally

Shreyas Bhaban and Murti Salapaka are with the Department of Electrical Engineering, University of Minnesota, Minneapolis, MN, 55455 USA

Saurav Talukdar is with Department of Mechanical Engineering, University of Minnesota, Minneapolis, MN, 55455 USA

Subhrajit Roychowdhury is with General Electric Global Research Centre, Niskayuna, NY 12309 USA

Mingang Li and Thomas Hays are with Department of Genetics Cell Biology and Development, University of Minnesota, Minneapolis, MN, 55455 USA

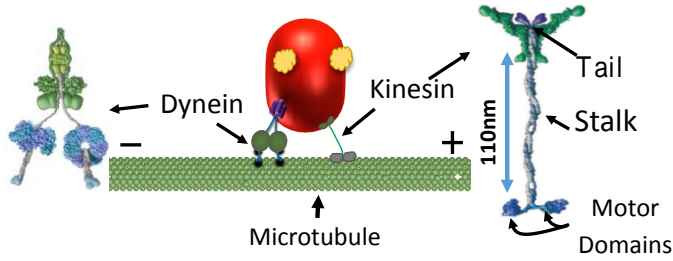


Fig. 1. Schematic showing intracellular cargo carried by motor proteins kinesin and dynein over a section of the microtubule inside the cell. Kinesin pulls the cargo towards the 'plus' end of the microtubule while dynein primarily pulls the cargo towards the 'minus' end of the microtubule

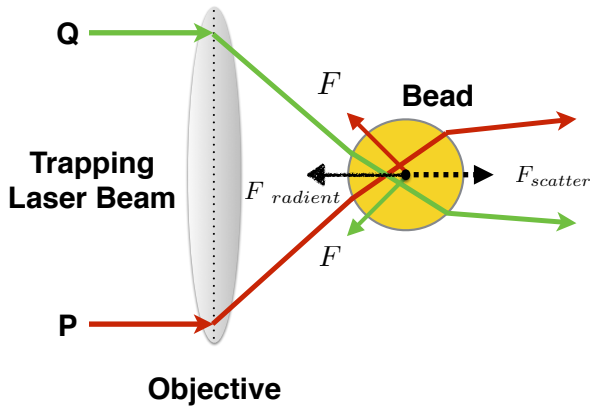


Fig. 2. Bead in an optical trap, as described in [7]. When the trapping laser beam is passed through a high numerical aperture objective, microscopic particles (such as the spherical bead) in the vicinity of the focus of the objective experience two kinds of forces (scattering and gradient forces) due to the momentum transfer onto the particles from the reflected and refracted rays of the laser. The destabilizing *scattering forces* generated by the laser beam are balanced by the *gradient forces* resulting from the Gaussian intensity profile of the laser; thereby creating a stable equilibrium point.

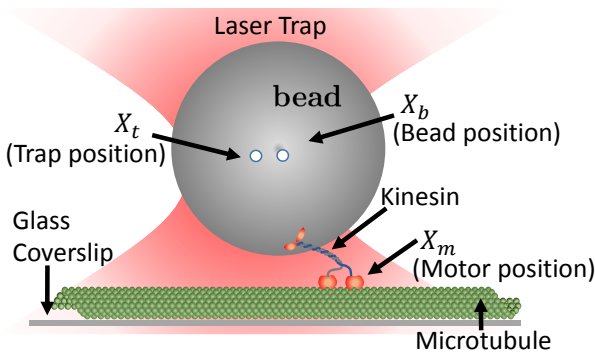


Fig. 3. Investigation of bead attached to motor protein 'kinesin' using an optical trap.  $X_t$ ,  $X_b$  and  $X_m$  denote the trap location, bead position and motor position respectively.

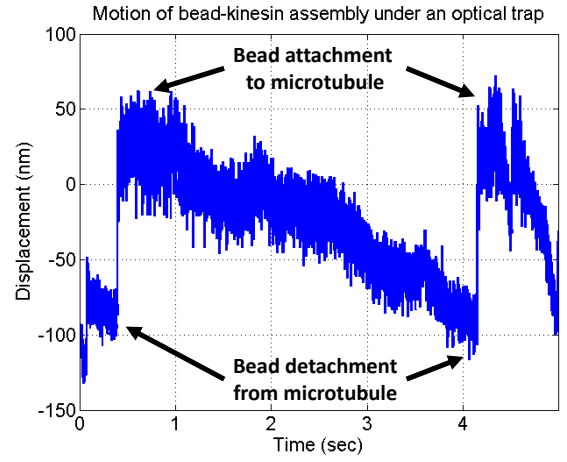


Fig. 4. Bead position data  $X_b$  gathered using position sensor, with the bead in an optical trap while simultaneously traversing along the microtubule via the motor protein kinesin attached to it. When the optical trap is held stationary, it exerts more and more force on the bead as the bead is pulled further away from the trap focus. With increasing force on the bead it is likely that the motors pulling the bead detach from the microtubule, at which point the bead is pulled back towards the focus of the trap due to the restoring force of the trap. The sawtooth-like patterns [8] characteristic of the bead motion due to the molecular motors attached to it are seen in this figure.

displacement  $\Delta x$  from the equilibrium point, the trap exerts a restoring force  $F_{trap}$  on the bead (directed towards the trap location) that varies linearly with the displacement, following the relationship  $F_{trap} = K_t \Delta x$ ; where  $K_t$  is the stiffness of the trap. The motion of the bead is typically detected using sensors such as photo-diodes or high speed cameras, that provide position accuracies ranging from micrometers to nanometers [12], [13]. The position of the bead can be controlled by manipulating the position of the trapping laser, using actuators such as galvo mirrors (with bandwidth in Hz) and acousto-optic deflectors (with bandwidth in KHz). Optical traps have enabled force resolution in femto newtons and position resolution in nanometers, proving immensely successful in the study of a variety of nano-scale systems such as transport inside cells [9], [14], separation of microscopic objects [15], [16], etc.

To facilitate the investigation of motor proteins and detection of the stepping motion (denoted by  $X_m$  in Fig. 3) using optical traps, motor proteins are attached to spherical dielectric beads using appropriate biochemical protocols (see [17]). The beads act as artificial cargoes that can be trapped using an optical trapping setup. An *in-vitro* environment mimicking the habitat inside the cell is created in a glass chamber, where microtubule filaments are coated at the base of the glass chamber. Using the principles of optical trapping (as shown in Fig. 2), the artificial cargo is trapped and brought close to the microtubules, to allow for the motor proteins connected to the cargo to attach to the microtubule as shown in Fig. 3. Once attached, the motor protein takes discrete steps on the microtubule, while pulling the bead. A sample of the bead position measured by a photo-diode sensor is shown in Fig. 4. The data enables inference of important statistics of molecular motors such

as motor detachment rates, stepping rates and reattachment rates, which inform several widely used models of motor proteins. The models have enabled numerous important results on intracellular transport by single and multiple motor proteins [18], [19], [20], [21].

Although measured bead position (such as that shown in Fig. 4) captures stepping statistics of the attached motor proteins, the motor linkage demonstrates non-linear characteristics and typically stiffens under increasing load [22], [23]. Thus, the bead displacements reflect but *do not exactly equal* the motor displacements and require variable corrections (about 15% for forces beyond 1 pN) to compensate for the effect [23]. Furthermore, for bead position measurements such as those as shown in Fig. 4, the restoring force on the bead varies as it travels under the influence of the trap. Thus the motor takes every step under changing load conditions. Transport properties of motor proteins are known to be altered under varying external loading conditions; thus making it cumbersome to study the effect of load forces on motor protein behavior.

Studies of molecular motors using optical tweezers under constant forces have been possible through the use of *constant force clamps* ([23], [24]), that are designed to make the optically trapped bead follow the motor protein motion by regulating the separation between bead and trap position ( $X_b - X_t$ ) to a desired value; thereby allowing for the approximation of motor linkage as a Hookean spring. It is equivalent to maintaining load force on the bead equal to  $F_d = K_t(X_b - X_t)$ , thus allowing for constant force studies. Furthermore, it enables the measured bead position to correctly reflect the motor motion; from which the motor stepping statistics can be extracted using a variety of offline step detection techniques [25], [26] without the need for ad-hoc corrections [23]. Constant force clamps typically operate by manipulating the position of the trap  $X_t$  (using the suitable actuators) to follow the bead, based on the measured bead position  $X_b$ . By integrating trap control with the ability to measure the position of the bead, it is possible to design closed loop feedback strategies that modulate the trap to regulate the load force on the bead close to desired force  $F_d$ .

A key challenge in maintaining constant load force using constant force clamp lies in achieving the desired outcome of force regulation in the presence of disturbances and thermal noise. The disturbance enters the system in the form of motor displacement  $X_m$ , which varies in speeds from a few nanometers per second to microns per second. Moreover, the noise signal at the scales where molecular motors function is comparable to the motor stepping signal. State-of-art force clamps [23], [24] are known to have low bandwidths and are only effective for slow stepping motors. They prove ineffective at regulating the trapping force on fast moving motors. Furthermore, force clamps are known to suffer from occasional instability arising from lack of formal controller design methodology as well as negligence of instrument dynamics. On the other hand since the measured bead position is highly corrupted with noise, accurate estimation of motor motion statistics cannot be made based on bead position; requiring post-processing using variety of offline methods [25], [26]. Presently, there is no method to provide to provide a real time

estimate of the motor stepping motion  $X_m$ . Therefore, accurate detection of stepping motion must not only involve a precise regulation of load force but also the reduction of noise effects on the step estimate. Current state-of-art [23], [24] is unable to accommodate such a multi-objective design, necessitating the need for a robust control design framework.

*Our Contribution:* In this article, we resort to the mixed objective  $H_2/H_\infty$  framework described in [27] to enable the accommodation of the desired diverse set of objectives. Using the framework, it is possible to have regulation of load force as a primary objective, while the accurate estimation of stepping motion forms the secondary objective. Regulation of load force is attained by reducing the  $H_\infty$  norm of the regulation error from the disturbance  $X_m$  and set point  $F_d$ . Accurate estimation of motor motion is attained by minimizing the  $H_\infty$  norm of the estimation error from the disturbance  $X_m$  as well as reducing the effects of thermal noise on step estimate by minimizing the  $H_2$  norm of motor motion estimation from thermal noise (white noise). Using this paradigm, we are able to achieve the dual objectives of force regulation and real time estimation of motor motion. Through numerical simulations, we demonstrate the ability to regulate forces below 1 pN with errors below 10% on motors moving up to speeds of 160 nm/s. It would enable constant force studies where low errors in force regulation is of critical importance [20], [19]. Furthermore, we are able to regulate forces on motors moving as fast as 1  $\mu\text{m/s}$  with errors below 17%, resulting in significantly improved force clamp capabilities for probing motors with larger step sizes (hence higher speeds [28]) and motors moving at native speeds [29]. Such objectives of regulating sub-piconewton load forces on low and high speed motors were not achievable before. Additionally, we are able to estimate motor motion in real time for motors travelling at speeds up to 120 nm/s with rms error in step estimation below 5%; while simultaneously maintaining sub pico-newton forces with regulation error below 10%.

We further implement the design on a custom designed optical tweezer setup and demonstrate the performance on live samples of motor protein ‘kinesin’. Experimentally, we are able to regulate forces below 1 pN with errors below 8% on motors moving up to 200 nm/s using *in-vitro* motility assays. Without sacrificing force regulation, we demonstrate real time stepping estimate of motor motion upto 108 nm/s. This constitutes first such demonstration, in both simulations and experiments, of maintaining load forces below 1 pN with errors less than 10% while simultaneously estimating motor motion in real time. A preliminary simulation study of the force clamps using robust control framework has previously appeared in [30] and a preliminary experimental demonstration of the force clamp on an system mimicking the motor motion has appeared in [31]. This article builds upon [30], [31] and additionally presents a detailed computational and experimental implementation of the constant force clamp on live motor protein (kinesin) samples. It provides first such demonstration of a model based control design framework on live motor protein samples.

The article is organised as follows. Section II presents the mathematical modeling and characterization of the system. Section III presents the controller design using the mixed

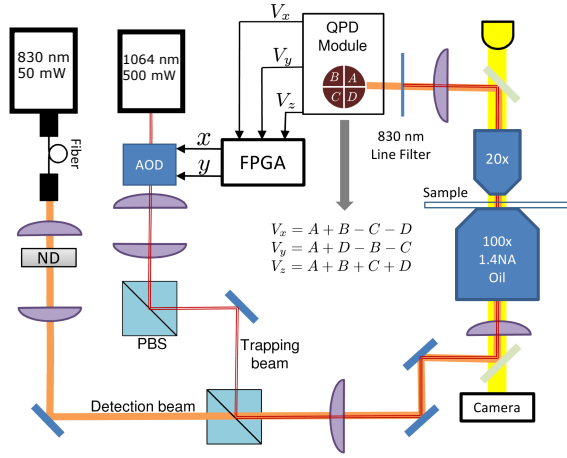


Fig. 5. Schematic for custom designed 'Optical Tweezer' setup

objective  $H_2/H_\infty$  described in [27] for the optical tweezer system. Here, we present simulation results for force regulation and real-time stepping estimation of motor motion in the presence of thermal noise. Section IV presents experimental implementation of the framework and the results associated with testing the design on live kinesin motor proteins. It is followed by section V and VI with discussions and conclusions.

## II. MODELING AND CHARACTERIZATION

### A. Experimental Setup

The experimental setup for realizing optical traps is a custom built optical tweezer setup (Fig. 5) where a Nd:YAG trapping laser (CrystaLaser Inc.,  $\lambda = 1064\text{nm}$ ,  $500\text{mW}$ ) is expanded using appropriate optics to fill the back aperture of high numerical aperture (NA) objective (Nikon 100x, 1.4 NA, oil immersion). The optical trap is formed at the focal point where spherical polystyrene beads are trapped. The trapping laser passes through 2-axis acousto-optic-detector (AOD, IntraAction Corp., *DTD-274HA6*) that precisely steers the beam in x-y plane in response to appropriate commands. To detect the bead position, a second detection laser (Point Source Inc., *iFLEX 2000*,  $50\text{mW}$ ,  $\lambda = 830\text{nm}$ ) is used to map the image of the bead onto a quadrant photodiode (QPD, Pacific Silicon Sensors, *QP50-6SD2*). A neutral density (ND) filter is added in the path of the detection laser to reduce its intensity to ensure that it doesn't interfere with the trapping phenomenon. The photodiode enables the detection of the bead location by providing three signals  $V_x$ ,  $V_y$  and  $V_z$  where  $V_x$  and  $V_y$  represent the light distribution on the photodiode along  $x$  axis and  $y$  axis respectively while  $V_z$  corresponds to total light intensity. These signals are captured using FPGA based data acquisition system (National Instruments, *PCI7833R*) that generates appropriate commands for the AOD. The controller is implemented using Labview-based NI-FPGA.

### B. System Model and Instrument Dynamics

Let the locations of the trap centre, cargo and motor head (on the microtubule) be denoted by  $X_t$ ,  $X_b$  and  $X_m$  respectively.

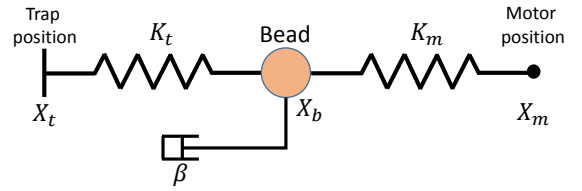


Fig. 6. Block diagram describing the open loop plant

The bead in the optical trap is suspended in an aqueous medium with the coefficient of viscous damping  $\beta$ . For small magnitudes of displacement  $X_b - X_t$  of the optically trapped cargo from the trap centre, the force on the bead due to the optical trap is given by  $K_t(X_b - X_t)$  [23]. Similarly, for small extensions  $X_m - X_b$  of the motor stalk, the force on the cargo due to the motor protein is modeled as  $K_m(X_m - X_b)$  [23], where  $K_m$  is the stiffness of the motor stalk linkage. Under these conditions, the molecular motor carrying an optically trapped cargo (in this case, a spherical dielectric bead) can be modeled as a spring-mass-damper system with trap stiffness  $K_t$ , motor stiffness  $K_m$  and the coefficient of viscous damping  $\beta$ , as shown in Fig. 6. The dynamics of the bead are observed to be highly over-damped [7], thus enabling the equation of motion of the bead in the presence of thermal noise  $\eta$  to be given by the following Langevin equation,

$$\beta \dot{X}_b = K_m(X_m - X_b) + K_t(X_t - X_b) + \eta. \quad (1)$$

Applying Laplace transform to Eq. (1),

$$X_b(s) = G(s)(K_m X_m(s) + K_t X_t(s) + \eta(s)). \quad (2)$$

where  $G(s) = \frac{1}{\beta s + K_t + K_m}$ .

In the absence of the disturbance (motor motion) and process noise (thermal noise), the bead position in open loop follows the equation  $\beta \dot{X}_b = K_t(X_t - X_b)$ , which after Laplace transform leads to  $X_b(s) = \frac{K_t}{\beta s + K_t} X_t(s)$ . The trap position  $X_t(s)$  can be manipulated using the command signal  $u(s)$  through the relation  $X_t(s) = A(s)u(s)$ , where the transfer function  $A(s)$  models the dynamics of the actuator used to control the trap position. For a good controller design, it is essential to take into account the effects of the instrument dynamics [32], [33], which captures the dynamics of the actuator as well as the control hardware. Thus, the position of the bead in open loop, in response to the command signal  $u(s)$  is given by,

$$X_b(s) = G_p(s) K_t A(s) u(s). \quad (3)$$

where  $G_p(s) = \frac{1}{\beta s + K_t}$ .

### C. Actuator Characterization

As mentioned earlier, one of the main objectives of our article is the estimation of motor stepping motion  $X_m$  through constant force clamps. The efficacy of the force clamp depends on its disturbance rejection bandwidth, with the disturbance being the stepping motion of the motor  $X_m$ . Existing state-of-art force clamps [23], [24] are constrained by their low

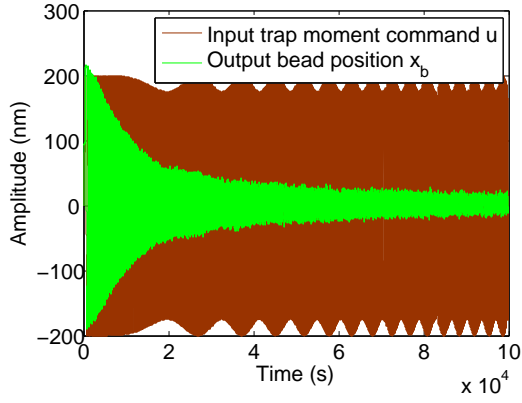


Fig. 7. System identification using chirp waveforms. Red traces denote the command input  $u$  while green traces denote the measured bead position  $X_b$ .

bandwidths and are only effective for analyzing slow motors; thereby failing to provide effective results for fast motors.

One of the primary reasons for the low bandwidth of the state-of-art force clamps is due to the fact that the actuator dynamics are not modeled properly. The acousto-optic deflector (AOD), which is typically used to manipulate the trap position in optical trapping systems, uses sound waves to create a diffraction grating in a crystal. The nature of the diffraction grating depends upon the frequency of the sound wave used, which is controllable using an input radio frequency (RF) wave. After the sound wave passes through the crystal, it is absorbed by an acoustic absorber. The laser used to create the optical trap is passed through the grating and the first order diffracted spot is utilized to create the optical trap. The spacing of the diffraction grating is altered by changing the frequency of the input RF wave, thereby affecting the position of the trap. It is evident that the position of the laser spot does not change until the sound wave has crossed the entire laser beam width, making the response time of the AOD dependent upon the speed of the sound wave and the laser beam width. Furthermore, the sound waves suffer from partial reflection from the boundaries of the crystal. Thus, a mixture of waves with different frequencies exists in the crystal after the input frequency is altered. The laser spot settles to the desired position only after the reflected waves completely die out. Therefore, the response time of the AOD is dependent on the time taken for the reflected waves to die out as well as the absorbing capacity of the acoustic absorber; which results in an inherent delay in the actuator.

It is clear that the delays present in the AOD dynamics due to its inherent physics need to be modeled precisely in order to design a force clamp that can accommodate slow as well as fast motors. In eq. (3), the transfer function from the command input  $u(s)$  to the measured bead position  $X_b(s)$  is given by  $G_h(s) = G_p(s)K_t A(s)$ . We determine the expression for the actuator transfer function  $A(s)$  from the experimentally identified expression for  $G_h(s)$  by using

$$A(s) = \frac{G_h(s)}{K_t G_p(s)}, \quad (4)$$

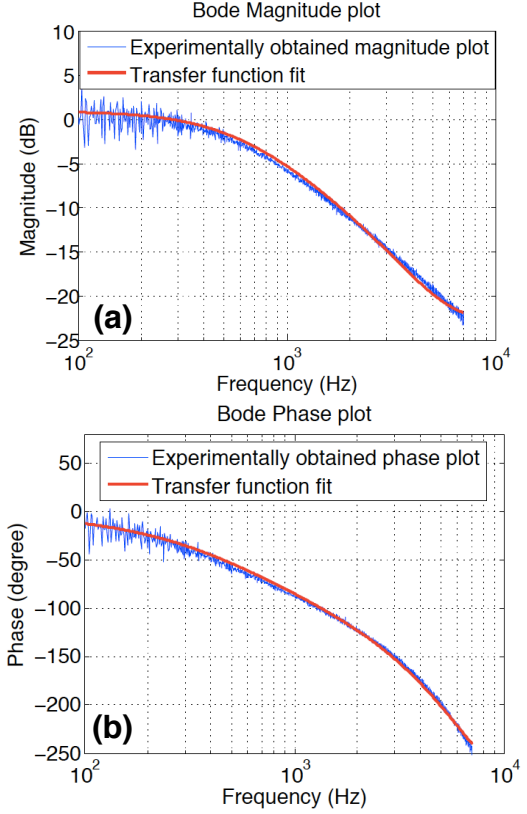


Fig. 8. Experimentally obtained (a) magnitude and (b) frequency plots for transfer function  $G_h(s)$  are shown by the 'blue' traces. The 'red' traces indicate a 3-pole 2-zero transfer function fit.

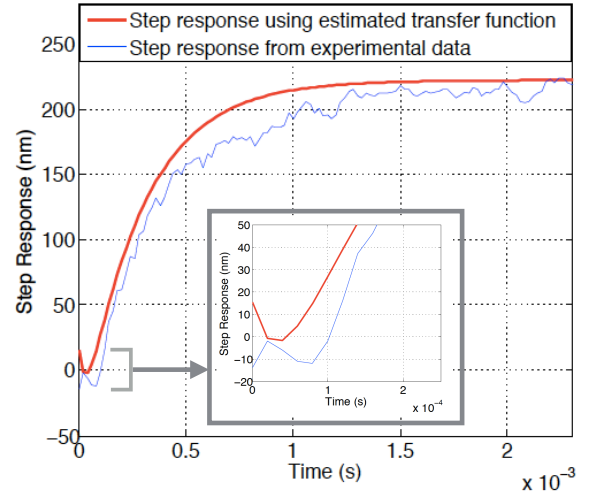


Fig. 9. Validation of the fitted transfer function  $G_h(s)$  by comparing step responses. The experimentally obtained step response shows close agreement with that obtained using the fitted transfer function  $G_h(s)$ . Note the undershoot seen in both the experimental and simulation data (see inset) is characteristic of the delays present in the AOD system.



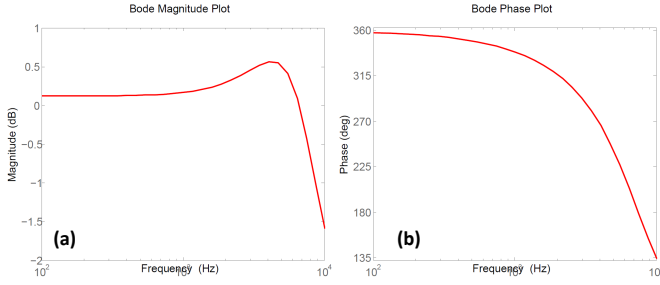


Fig. 10. Magnitude and phase plots for identified transfer function of the actuator,  $A(s)$ . Note that at high frequencies, magnitude reduces and phase delay increases, affecting the actuator response for input signals at high frequencies.

where trap stiffness  $K_t$  and damping coefficient  $\beta$  are obtained by methods described in [23]. To identify  $G_h(s)$  specific to the actuator and control hardware used to perform the experiments in this article, we perform a chirp-wave based system identification where the input signal  $u(t)$  is a sinusoidal wave of varying frequencies and output signal is the bead position  $X_b(t)$  as shown in Fig. 7. Subsequently, the ratio of amplitudes and the phase difference between the output signal  $X_b(j\omega)$  and input signal  $u(j\omega)$  is obtained as shown in Fig. 8(a) and Fig. 8(b) respectively. A 3-pole 2-zero transfer function fit yields  $G_h(s) = \frac{0.0396s^2 - 3160s + 1.101 \times 10^8}{1.7 \times 10^{-5}s^3 + 0.9967s^2 + 3.408 \times 10^4s + 1.086 \times 10^8}$ . The experimentally obtained model using the frequency response is accurate, which is demonstrated in Fig. 9 where the experimentally obtained step response shows a good match with the response predicted by the fitted transfer function  $G_h(s)$ . Fig. 9(blue curve) clearly demonstrates that the bead initially traverses in a direction opposite to the commanded direction, which is characteristic of the delays present in the actuation system. The identified transfer function  $G_h(s)$  (shown in Fig. 9, red curve) contains a right half plane zero, thus appropriately capturing the effect of the delays; and by using eq. 4 yields the actuator transfer function  $A(s) = \frac{0.66s^2 - 5.267 \times 10^4s + 1.835 \times 10^9}{s^2 + 5.5 \times 10^4s + 1.8 \times 10^9}$ .

The magnitude and frequency plots of  $A(s)$  are shown in Fig. 10(a) and (b) respectively. It is evident that at higher frequencies, the gain reduces and the phase delays become significantly larger; implying that at higher frequencies the trap position will not instantaneously move by the desired magnitude when commanded. Existing force clamps [23], [24] make the simplifying assumption of  $A(s) = 1$  which is only appropriate for low frequencies and will lead to diminished performance at higher frequencies. Thus, utilizing experimentally determined model for the actuation system  $A(s)$  improves the disturbance rejection bandwidth of the subsequently designed force clamp.

Equipped with the knowledge of the actuator dynamics, a block diagram describing of the open loop plant  $P_{OL}$  can be described as shown in Fig. 11. In the next section, we present the mixed objective  $H_2/H_\infty$  framework utilized in order to design a controller that meets the multiple objectives of maintaining constant force on the bead and estimating the disturbance signal (motor stepping motion).

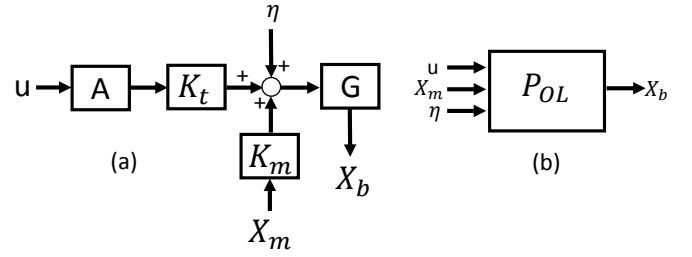


Fig. 11. Block diagram of the open loop plant  $P_{OL}$ . The inputs to the plant are  $u$ ,  $X_m$  and  $\eta$  which denote the trap moment command, motor motion and thermal noise respectively. The output  $X_b$  denotes the bead position as measured by the photo diode. As mentioned earlier,  $G(s) = \frac{1}{\beta s + K_t + K_m}$  and  $A(s)$  denotes the transfer function from trap command signal  $u(s)$  to the trap position  $X_t(s)$ , thereby capturing the dynamics of the actuator (AOD).

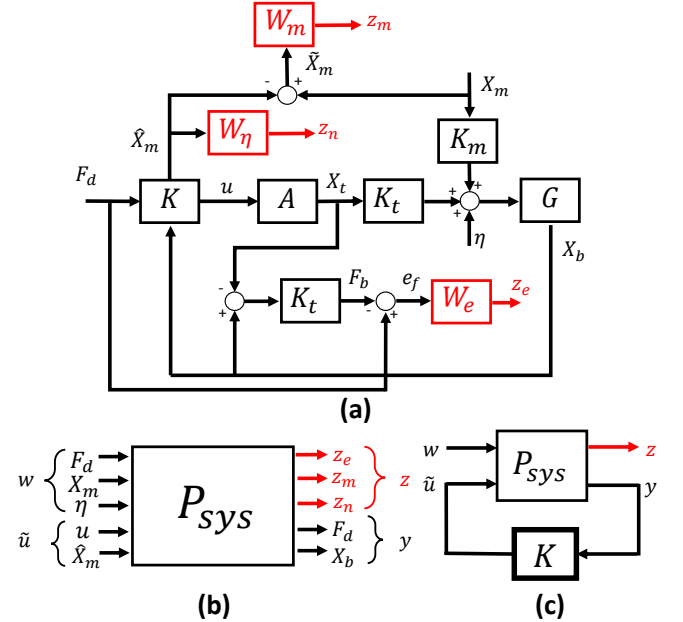


Fig. 12. (a) Block diagram of the plant with frequency dependent weights  $W_e$ ,  $W_m$  and  $W_\eta$ . (b)  $P_{sys}$  denotes the transfer function of the system with inputs  $[w; \tilde{u}]$  and outputs  $[z; y]$ . (c) Closed loop representation of the system with controller  $K$ .

### III. CONTROLLER SYNTHESIS

As alluded to in the earlier sections, a constant force clamp requires that a constant force be maintained on the bead in the presence of disturbances (such as motor motion  $X_m$ ) and process noise (thermal noise  $\eta$ ) as shown in Figure 12 (a). The presence of disturbance and process noise necessitates the use of feedback control strategies for maintaining a constant force of  $K_t(X_b - X_t)$  on the bead. The feedback signal utilized is the measured position of the bead  $X_b$ . The other task is to estimate the disturbance input (motor motion  $X_m$ ) to the plant in real time using  $X_b$ . A block diagram explaining the various components of the optical trapping system together with the feedback controller  $K$  is shown in Fig. 12 (a). The controller takes the desired force  $F_d$  and the measured bead position  $X_b$

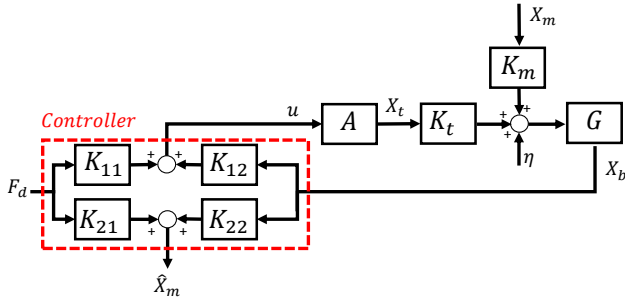


Fig. 13. Block diagram describing the closed loop plant with open loop plant  $P_{OL}$  and controller  $K$ .

as its inputs and provides the command signal to the AOD  $u$  and the estimate  $\hat{X}_m$  of the disturbance  $X_m$  as its outputs, thus, the controller  $K(s)$  is a two-input two-output system as shown in Fig. 13. Note that, in the given system,  $X_t$  is not measured; hence, it is not possible to design a feedback strategy which uses regulation error  $e_f$  as an input to the controller. The proposed framework enables desired objectives to be obtained without resorting to the regulation error  $e_f$ . The performance objectives, in the order of priority to be achieved by the closed loop system are as follows:

- 1) ‘Good’ ( $< 10\%$ ) force regulation in the presence of disturbances and set point changes
- 2) ‘Accurate’ ( $< 8$  nm rms estimation error) real time estimation of motor motion

The first objective above translates to a requirement of ‘small’ gain for the transfer functions  $T_{e_f F_d}(s)$  and  $T_{e_f X_m}(s)$ , where  $T_{e_f F_d}(s)$  and  $T_{e_f X_m}(s)$  denote the transfer function from  $F_d$  to  $e_f$  and  $X_m$  to  $e_f$  respectively. The second objective translates to a ‘small’ gain for the transfer functions  $T_{\hat{X}_m X_m}(s)$ , where,  $T_{\hat{X}_m X_m}(s)$  is the transfer function from the disturbance  $X_m$  to disturbance estimation error  $\hat{X}_m$ . The presence of the effect of thermal noise in the plant output  $X_b$  necessitates filtering out the effect of the white noise from the disturbance estimate  $\hat{X}_m$ . This translates to reducing the effect of  $\eta$  (white noise) on  $\hat{X}_m$ , that is, minimize the gain of  $T_{\hat{X}_m \eta}(s)$  across all frequencies, where  $T_{\hat{X}_m \eta}(s)$  is the transfer function from thermal noise  $\eta$  to the disturbance estimate  $\hat{X}_m$ . Note that the disturbance  $X_m$  and the process noise  $\eta$  enter at the same location as shown in Figure 12 (a), so minimizing the  $H_2$  norm of  $T_{\hat{X}_m \eta}(s)$  is the same as minimizing the  $H_2$  norm of  $T_{\hat{X}_m X_m}(s)$ .

#### A. Design Objectives

It is clear from the above discussion that the desired performance is multi-objective and involves specific input output channels of the generalised plant. The multi-objective output feedback control paradigm laid out in [27] provides an effective controller synthesis approach to meet the desired objectives. The list below enumerates the desired performance requirements in control theory terminology.

- 1) minimize  $\| [T_{e_f F_d} \ T_{e_f X_m}] \|_{H_\infty}$
- 2) minimize  $\| T_{\hat{X}_m X_m} \|_{H_\infty}$

- 3) minimize  $\| T_{\hat{X}_m X_m} \|_{H_2}$

A key feature of the LMI based control synthesis (convex optimization problem) framework presented in [27] it that it allows to optimize for specific input-output channel performance. Our approach minimizes the  $H_\infty$  norm of the transfer functions in (1) and (2) above, and incorporates (3) as a constraint  $\| T_{\hat{X}_m \eta} \|_{H_2}^2 < \nu$  in the optimization problem, where  $\nu$  is specified by the user. Incorporating the 3<sup>rd</sup> objective as a constraint helps avoid feasibility issues. Furthermore, frequency dependent weights  $W_e(s)$ ,  $W_m(s)$  and  $W_\eta(s)$  are introduced to penalize the signals  $e_f$ ,  $\hat{X}_m$  and  $\hat{X}_m$  respectively as shown in Figure 12 (a) and ensure feasibility of the optimization problem. Note that,  $W_m(s)$  and  $W_\eta(s)$  should emphasize non-overlapping frequency regions since the signals  $X_m$  and  $\eta$  enter the plant at the same location. We define the vector  $z := [z_e, z_m, z_\eta]^T$  as the generalized output vector,  $w := [F_d, X_m, \eta]^T$  as the vector of generalised input,  $y := [F_d, X_b]^T$  as the input to the controller and  $\tilde{u} := [u, \hat{X}_m]^T$  as the output of the controller  $K$  and  $P_{sys}$  is the open loop plant including the weights, as shown in Figure 12 (b) (see Appendix C for details). The weighted performance objectives are given as:

- (a) minimize  $\| [T_{z_e F_d} \ T_{z_e X_m}] \|_{H_\infty}$
- (b) minimize  $\| T_{z_m X_m} \|_{H_\infty}$
- (c)  $\| T_{z_\eta X_m} \|_{H_2}^2 < \nu$

The associated optimization problem to synthesize a controller  $K(s)$  which is optimal with respect to (a), (b) and (c) is given below as,

$$\begin{aligned} & \min_{K(s), \gamma} \gamma \\ & \text{such that, } \| [T_{z_e F_d} \ T_{z_e X_m}] \|_{H_\infty} < \gamma \\ & \| T_{z_m X_m} \|_{H_\infty} < \gamma \\ & \| T_{z_\eta X_m} \|_{H_2}^2 < \nu \end{aligned}$$

The above optimization problem can be formulated as a convex optimization problem as shown in [27] and optimal solution to which is obtained by solving the LMIs (6-10) listed in the Appendix D. The solution scheme utilizes a common Lyapunov function for all three objectives, thereby bringing some amount of conservatism in the design process. However, the obtained controller is guaranteed to be stabilizing and most importantly it is of the same order as the plant, thus, suitable for real time implementation in this case. The associated closed loop system is shown in Fig. 12 (c).

The weight  $W_e(s)$  is chosen to penalize the regulation error  $e_f$ , with gains below  $-16$  dB for disturbances upto 150 Hz, corresponding to average motor velocity of 1200  $\mu\text{m/s}$ . It ensures small values of regulation errors at steady state as well as the frequencies of interest, corresponding to the observed native speeds of molecular motors [29].  $W_m$  is chosen to minimize the effect of disturbances on estimation of motor motion, for motor speeds upto 160  $\text{nm/s}$ , consistent with observed *in-vitro* speeds using the motility protocol designed in [17] (further details are provided in next section).  $W_\eta(s)$  is chosen to penalize the higher frequencies ( $> 20$  Hz) so that the estimate  $\hat{X}_m$  is devoid of high frequency noise.  $W_\eta(s)$  is

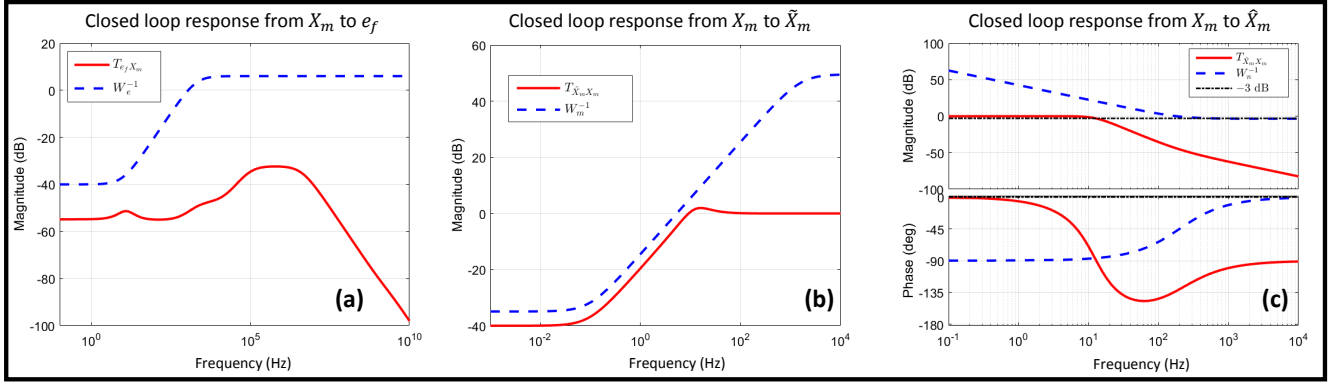


Fig. 14. Frequency response of (a)  $T_{e_f X_m}(s)$  and  $W_e^{-1}(s)$ , (b)  $T_{\hat{X}_m X_m}(s)$  and  $W_m^{-1}(s)$ , (c)  $T_{\hat{X}_m X_m}(s)$  and  $W_n^{-1}(s)$  using mixed objective  $H_2/H_\infty$  method. All three closed loop transfer functions meet the desired frequency dependent performance for the chosen weights  $W_e = \frac{0.5s+6000}{s+60}$ ,  $W_m = \frac{0.01s+100}{3s+1.8}$  and  $W_n = \frac{1.194 \times 10^{-3}s}{7.958 \times 10^{-4}s+1}$ .

also chosen such that it avoids an overlap of frequencies with the chosen weight  $W_m(s)$ , while also ensuring the feasibility of the optimization problem. The  $2 \times 2$  controller  $K(s)$  is determined using the given frequency dependent weights and  $\nu$  ( $= 2.23$ ) by solving the corresponding LMIs (using CVX [34]). The optimal value of  $\gamma$  is obtained to be 0.67. The frequency response of the inverse of the weights  $W_e(s)$ ,  $W_m(s)$ ,  $W_n(s)$  and the corresponding closed loop transfer functions are shown in Figure 14. Clearly, the closed loop transfer functions meet the desired frequency dependent performance specifications.

### B. Simulation results

The performance comparison metric for regulation is the percentage regulation error,  $r := \frac{\sigma(F_d - K_t(X_b - X_t))}{F_d} \times 100$ , where  $\sigma(\cdot)$  denotes standard deviation. The performance metric for estimation error,  $e_{rms} := \sqrt{\langle \hat{X}_m^2 \rangle}$ , where  $\langle \cdot \rangle$  denotes the expectation operator. Table I lists the regulation and estimation error performance of the synthesized controller for  $F_d = 0.95$  pN and  $X_m$  being a simulated staircase signal of 8 nm steps with frequencies of 5, 10, 15, 20, 125 steps/sec. Figure 15 shows the estimate  $\hat{X}_m$  of  $X_m$  using the noisy bead position  $X_b$  when the frequency of the steps is 5 Hz (see Figure 15 (a) and (b)). It is seen from Table I that regulation is less than 10% and the rms estimation error is less than 6 nm for *in-vitro* motor stepping frequencies of upto 20 Hz. The regulation and disturbance estimation performance degrades for high speed motors as seen in the 125 steps/sec case. Thus, the synthesized controller achieves the desired objectives of force regulation and real-time motor motion estimation in simulation for motors moving at speeds around 160 nm/sec, with satisfactory force regulation for motors moving at higher speeds (around 1  $\mu\text{m/sec}$ ). In the next section the experimental performance of the controller.

## IV. EXPERIMENTS WITH LIVE MOTOR PROTEINS

In this section, we present an experimental implementation of the mixed objective  $H_2 - H_\infty$  optical force clamp (designed

TABLE I. REGULATION AND ESTIMATION ERROR FOR VARIOUS MOTOR STEPPING FREQUENCIES

Stepping Frequency (steps/sec)	Motor Speed (nm/s)	$r(\%)$	$e_{rms}(\text{nm})$
5	40	4.85	5.21
10	80	7.42	4.83
15	120	8.06	4.78
20	160	8.40	4.88

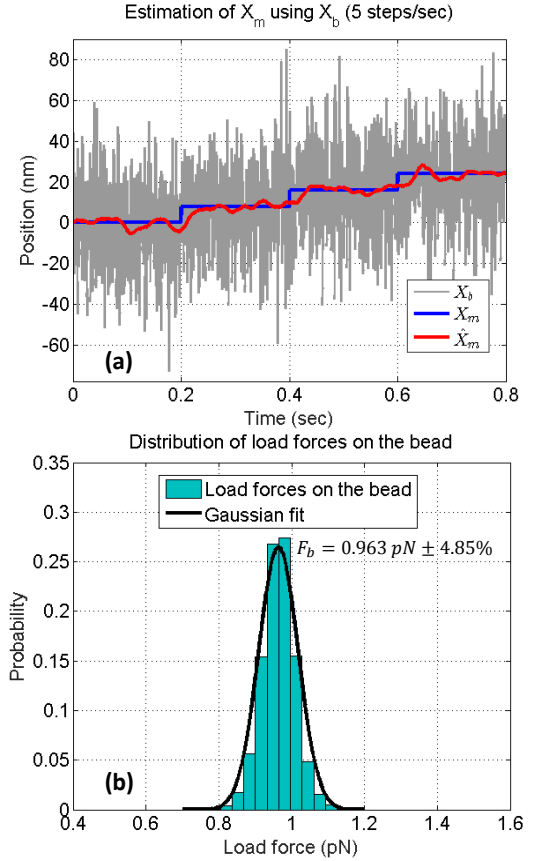


Fig. 15. (a) A realization of  $\hat{X}_m$  computed using  $X_b$  when simulated  $X_m$  is a staircase signal with stepping frequency 5 Hz and (b) the distribution of the associated regulation error. The force on the bead is  $F_b = 0.963 \text{ pN} \pm 4.85\%$ .



TABLE II.  $H_2 - H_\infty$  FORCE CLAMP REGULATION PERFORMANCE

Motor Speed in (nm/s)	Error in force regulation (%)
59.17	4.67
68.11	5.069
93.2	7.07
107.53	6.075
152.01	5.073
193.3	7.97

in the previous section) on our optical tweezer setup. The controller  $K$  is implemented using an National Instruments *PCI7833R* FPGA, with a brief description provided in Appendix B. Furthermore, we develop and implement a bead motility assay as described in [17] to provide carboxylated beads  $1\mu m$  in diameter attached to Kinesin-I motor protein. We then test the performance of the mixed objective clamp on the beads carried by live proteins and compare it with the performance of existing state-of-art force clamps, under the same conditions.

#### A. Procedure and demonstration

To investigate motor protein motion using an optical force clamp, the optical tweezer is utilized to trap a polystyrene bead, with the bead being attached to kinesin motors using the protocol described in [17]. The trapped bead is brought closer to the base of the glass slide where microtubule filaments have been previously coated (See [17] for details) and held stationary at a distance of about  $100\text{ nm}$  from it. As the kinesin protein gradually attaches to the microtubule and begins traversing, a unidirectional motion of the bead towards the positively charged end of the microtubule is recorded using the photodiode sensor (see Fig. 4)

The optical force clamp is designed to maintain a constant force of  $F_d$  on the bead, which is equivalent to maintaining a constant distance of  $d = X_b - X_t = \frac{F_d}{K_t}$  between the locations of the bead and the trap. The clamp is designed to trigger only after the bead has moved more than a distance of  $d$  away from the trap focus, that is, after  $(X_b - X_t \geq d)$ . When  $(X_b - X_t < d)$ , the force clamp is not triggered and the trap position does not change in response to changes in the bead position. An instance of the force clamp in action for  $d = 100\text{ nm}$  is demonstrated in Fig. 16 (a), where zones 1, 2 and 3 denote the different stages of study of bead motion under the optical force clamp. A representation of the bead-motor assembly corresponding to each of the zones is shown in Fig. 16 (b). In zone (1), the bead is trapped and being brought close to the microtubule, awaiting attachment of the motor. In zone (2), the motor attaches to the microtubule and pulls the bead, yet the force clamp is not triggered since  $(X_b - X_t < d)$ . In zone (3),  $(X_b - X_t \geq d)$  and the force clamp is triggered, where as seen in the corresponding section in the Fig. 16 (a), the trap position (red trace) follows the bead position (blue trace) and maintains the distance  $X_b - X_t$  close to  $d = 100\text{ nm}$ . For the trap stiffness  $K_t = 0.0095\text{ pN/nm}$ ,  $d = 100\text{ nm}$  translates to a desired force of  $F_d = 0.950\text{ pN}$  on the bead.

TABLE III. PERFORMANCE USING TRADITIONAL FORCE CLAMP [23]

Motor Speed in (nm/s)	Error in force regulation (%)
45.86	17.806
149.64	17.68

#### B. Results

The mixed objective  $H_2 - H_\infty$  force clamp was tested on beads with average velocities ranging from about  $59\text{ nm/s}$  to  $193\text{ nm/s}$  (see Table II for details). The mixed objective force clamp demonstrated excellent regulation performance, with the error in force resolution ranging from 4.67% to 7.97%. An instance of the force clamp operating on a bead travelling at  $107\text{ nm/s}$  is shown in Fig. 17 (a), where an error of in force regulation of 6.075% is obtained (as shown in Fig. 17 (b)). Note that, the data in table II is the first such demonstration where the force clamp has been able to obtain a force regulation as low as 4.67% while maintaining forces below  $1\text{ pN}$ . We compared the performance of the existing state-of-art [23] under similar conditions of load force and velocities, where higher errors in force regulation were seen (as shown in Table III). An instance of the traditional force clamp operating on a bead travelling at  $149\text{ nm/s}$  is shown in Fig. 18 (a), where an error of 17.68% is obtained (as shown in Fig. 18 (b)). It is evident that the mixed objective approach provides a significant advantage over the existing approaches and is capable of regulating sub  $pN$  forces with errors as low as 4.67%.

We further utilized the mixed objective force clamp to provide with a real time estimate  $\hat{X}_m$  of the motor motion  $X_m$ . The estimate of the motor motion for an average velocity of  $58.17\text{ nm/s}$  ( $\approx$  stepping frequency of 7 steps/sec) is shown by red curve in Figure 19. Since the actual stepping signal is not known, an estimate obtained using state-of-art offline step estimation algorithm [26] (blue curve) is shown for comparison. It is clearly seen that the high frequency noise is filtered out, providing an estimate  $\hat{X}_m$  comparable with state-of-art offline step estimation techniques. The motor motion estimation for higher average velocity of  $107.53\text{ nm/s}$  ( $\approx$  stepping frequency of 13 steps/sec) is demonstrated in Figure 20, which is also comparable with the estimates obtained using [26]. Note that, due to the presence of noise, the extraction of stepping data from the bead data is currently done using variety of offline techniques. Our method is the first of its kind that demonstrates estimation of motor motion in real time. The estimated signal  $\hat{X}_m$  provides starting points or edges that can be used by machine learning or dynamic programming based algorithms to generate statistics in real time or with an acceptable amount of delay. Thus, the force clamp presented in this article facilitates investigation and real time estimation of motor motion under sub  $pN$  load forces, a phenomenon which to the best of our knowledge has not been reported in the existing studies.

#### V. CONCLUSION

This article presents a computational and experimental verification of an *optical force clamp* designed using a mixed objective  $H_2/H_\infty$  framework, with extensive applications to

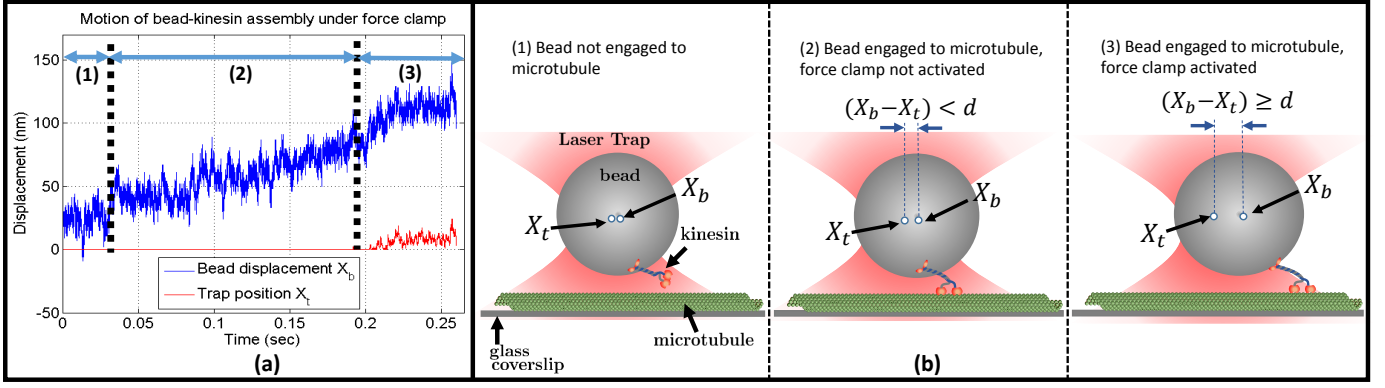


Fig. 16. (a) Sample trace of bead ( $X_b$ ) and trap position ( $X_t$ ) showing optical force clamp in action, divided into three zones. (b) Diagrammatic representation of the behavior of bead-kinesin ensemble in each of the three zones. In zone (1), the bead attached to kinesin is brought close to the glass surface and awaits the attachment of the kinesin to the microtubule filaments coated onto it. No motion of the bead is recorded as the kinesin does not attach to the microtubule. Once the attachment occurs as shown in zone (2), the motor pulls the bead and traverses along the microtubule in a directed manner. However, since the displacement of the bead position from the trap position is less than  $d = 100 \text{ nm}$ , the force clamp is not triggered and the trap position  $X_t$  remains unchanged. Once  $X_b - X_t > 100 \text{ nm}$  as seen in zone (3), the force clamp is triggered and the trap position follows the bead position while maintaining  $X_b - X_t$  close to  $100 \text{ nm}$ .

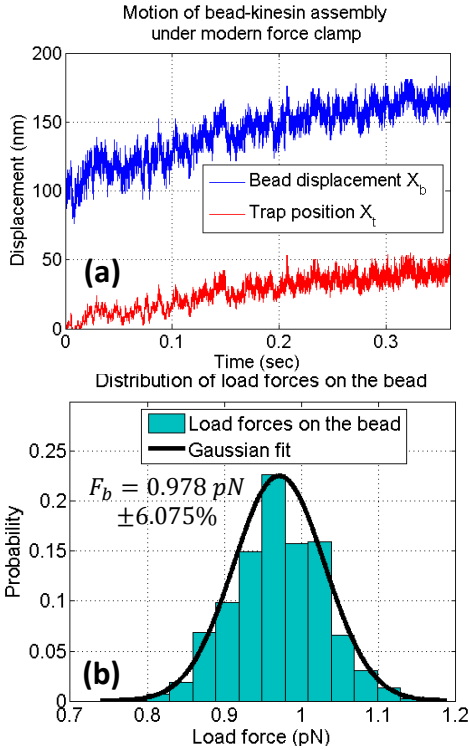


Fig. 17. (a) Sample trace of bead and trap position showing the modern  $H_2/H_\infty$  force clamp in action (b) Distribution of the error in force regulation.

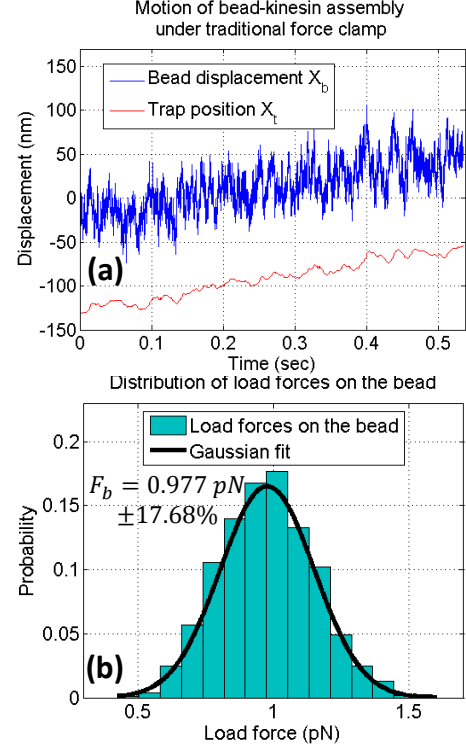


Fig. 18. (a) Sample trace of bead and trap position showing the traditional force clamp [23] in action (b) Distribution of the error in force regulation.

investigation of bio-molecules and processive motor proteins. The model-based approach using a systematic design methodology results in substantial improvement in force regulation and bandwidth of operation over existing designs [24], [23]. A crucial enabler of the design is a precise understanding and modeling of hitherto un-modeled delays in the existing instruments through right half plane zeros; identified using

a data-driven system identification approach. We verify the design through extensive numerical simulations, providing improved force regulation with guaranteed performances based on user-defined weight functions. The improved design can enable bio-molecular studies with higher resolution through the ability to investigate systems at finer intervals of forces. It will allow researchers to discover events that were not possible due

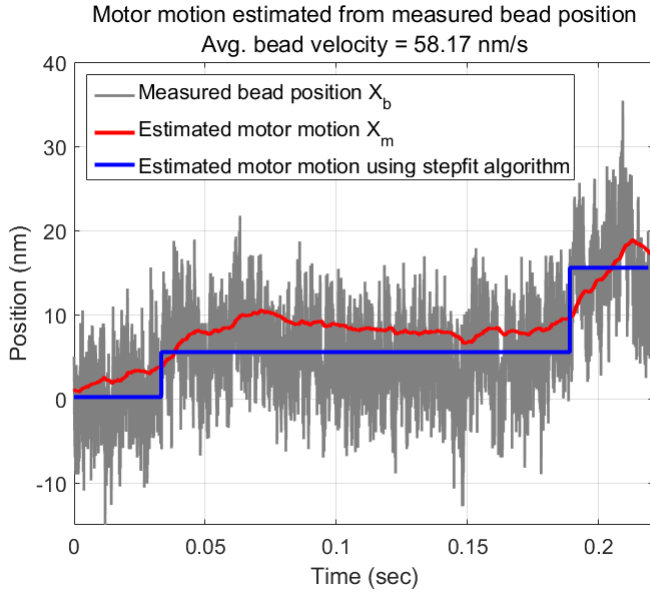


Fig. 19. Real time estimation of stepping motion, with average bead velocity of 58.17 nm/s

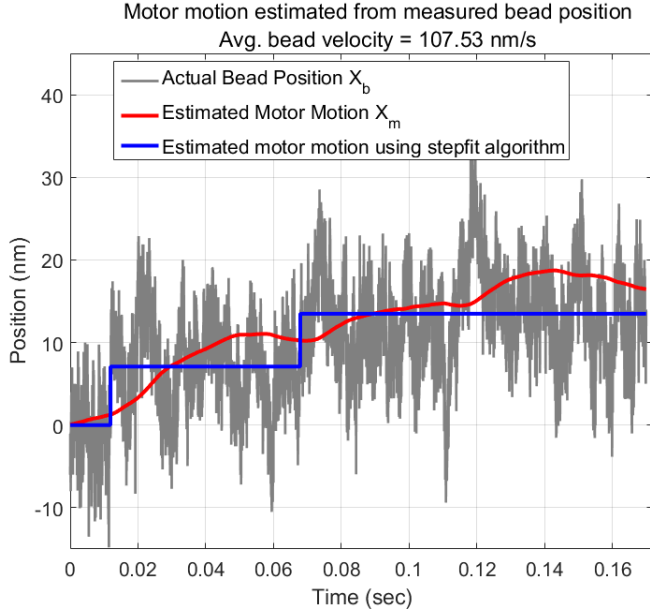


Fig. 20. Real time estimation of stepping motion, with average bead velocity of 107.53 nm/s

to limitations of current designs, leading to possible refinement of bio-molecular models. The design also allows for examining motor proteins at velocities close to their native speeds [29] and proteins with larger step sizes [28] with satisfactory force regulation. The design using modern control framework adds to the robustness of the system to parametric uncertainties. We further implemented the design on an optical tweezer setup and tested its efficacy using live samples of the motor protein ‘kinesin’, demonstrating the ability to regulate sub-pico newton forces with errors below 10%; individual attempts have also

shown errors below 5%.

The article also proposes a scheme for real time stepping estimation of molecular motors, which to the best of our knowledge is absent from current literature. By virtue of the mixed objective  $H_2/H_\infty$  design, we are able to reduce the effects of thermal noise on stepping estimate by bounding the  $H_2$  norm of the concerned channel and minimizing the  $H_\infty$  norm over step estimate error; without compromising on the force regulation. We demonstrate the efficacy of the method using simulations as well as experiments involving live ‘kinesin’ samples. Unlike some methods that reduce the thermal noise effects on stepping signal through stiffening the system [35], [23], our method preserves the dynamics of the system and thus avoids impacting the system being examined. The real time step estimation methodology can prove to be of tremendous importance to experimental biophysicists, equipping them with the ability to detect and identify motor protein motility in real time and avoiding the need for offline post-processing algorithms [25], [26]. Note that the step estimation bandwidth for our method is limited to about 20 steps/sec (corresponding to low motor speeds of kinesin of about 160 nm/s), due to the trade-off in the  $H_2/H_\infty$  cost over the identical channel. It is useful for motor proteins operating in the high load force and low ATP regimes [23], [36]. A possible scope for improvement is by exploiting the knowledge of the noise properties and designing the corresponding weight function ( $W_\eta$  in this article) more efficiently. Nevertheless, our proposed scheme enables improved investigative abilities in molecular biology using system theory tools and provides significant improvement in force clamping abilities over current methods, with the added contribution of estimation of motor motion in real time.

#### ACKNOWLEDGMENT

The authors would like to thank Tanuj Agrawal, Cymer for sharing his insights on optical tweezers. The discussions with Prof. Peter Seiler, Biswaranjan Mohanty and Sivaraman Rajaganapathy from the University of Minnesota have been insightful.

#### REFERENCES

- [1] E. L. Holzbaur and Y. E. Goldman, “Coordination of molecular motors: from in vitro assays to intracellular dynamics,” *Current opinion in cell biology*, vol. 22, no. 1, pp. 4–13, 2010.
- [2] J. P. Caviston and E. L. Holzbaur, “Microtubule motors at the intersection of trafficking and transport,” *Trends in cell biology*, vol. 16, no. 10, pp. 530–537, 2006.
- [3] K. Svoboda, C. F. Schmidt, B. J. Schnapp, and S. M. Block, “Direct observation of kinesin stepping by optical trapping interferometry,” *Nature*, vol. 365, no. 6448, p. 721, 1993.
- [4] C. L. Asbury, A. N. Fehr, and S. M. Block, “Kinesin moves by an asymmetric hand-over-hand mechanism,” *Science*, vol. 302, no. 5653, pp. 2130–2134, 2003.
- [5] M. A. Welte, S. P. Gross, M. Postner, S. M. Block, and E. F. Wieschaus, “Developmental regulation of vesicle transport in drosophila embryos: forces and kinetics,” *Cell*, vol. 92, no. 4, pp. 547–557, 1998.

- [6] G. A. Morfini, Y.-M. You, S. L. Pollema, A. Kaminska, K. Liu, K. Yoshioka, B. Björklom, E. T. Coffey, C. Bagnato, D. Han *et al.*, “Pathogenic huntingtin inhibits fast axonal transport by activating jnk3 and phosphorylating kinesin,” *Nature neuroscience*, vol. 12, no. 7, pp. 864–871, 2009.
- [7] S. Bhaban, S. Talukdar, and M. Salapaka, “Noise induced transport at microscale enabled by optical fields,” in *American Control Conference (ACC)*, 2016. IEEE, 2016, pp. 5823–5829.
- [8] K. Svoboda and S. M. Block, “Force and velocity measured for single kinesin molecules,” *Cell*, vol. 77, no. 5, pp. 773–784, 1994.
- [9] M. J. Schnitzer and S. M. Block, “Kinesin hydrolyses one atp per 8-nm step,” *Nature*, vol. 388, no. 6640, pp. 386–390, 1997.
- [10] J. A. Spudich, S. E. Rice, R. S. Rock, T. J. Purcell, and H. M. Warrick, “Optical traps to study properties of molecular motors,” *Cold Spring Harbor Protocols*, vol. 2011, no. 11, pp. pdb-top066662, 2011.
- [11] A. Ashkin, J. Dziedzic, J. Bjorkholm, and S. Chu, “Observation of a single-beam gradient force optical trap for dielectric particles,” *Optics letters*, vol. 11, no. 5, pp. 288–290, 1986.
- [12] T. Aggarwal, “Novel tools for biophysics research,” Ph.D. dissertation, UNIVERSITY OF MINNESOTA, 2012.
- [13] T. Aggarwal and M. Salapaka, “Real-time nonlinear correction of back-focal-plane detection in optical tweezers,” *Review of Scientific Instruments*, vol. 81, no. 12, p. 123105, 2010.
- [14] D. K. Jamison, J. W. Driver, and M. R. Diehl, “Cooperative responses of multiple kinesins to variable and constant loads,” *Journal of Biological Chemistry*, vol. 287, no. 5, pp. 3357–3365, 2012.
- [15] M. D. Wang, H. Yin, R. Landick, J. Gelles, and S. M. Block, “Stretching dna with optical tweezers,” *Biophysical journal*, vol. 72, no. 3, pp. 1335–1346, 1997.
- [16] Y. Cui and C. Bustamante, “Pulling a single chromatin fiber reveals the forces that maintain its higher-order structure,” *Proceedings of the National Academy of Sciences*, vol. 97, no. 1, pp. 127–132, 2000.
- [17] S. Roychowdhury, “Breaking perceived limits of performance for nanoscale interrogation & transport systems,” Ph.D. dissertation, UNIVERSITY OF MINNESOTA, 2015.
- [18] A. Kunwar, M. Vershinin, J. Xu, and S. P. Gross, “Stepping, strain gating, and an unexpected force-velocity curve for multiple-motor-based transport,” *Current biology*, vol. 18, no. 16, pp. 1173–1183, 2008.
- [19] D. Materassi, S. Roychowdhury, T. Hays, and M. Salapaka, “An exact approach for studying cargo transport by an ensemble of molecular motors,” *BMC biophysics*, vol. 6, no. 1, p. 14, 2013.
- [20] S. Bhaban, D. Materassi, M. Li, T. Hays, and M. Salapaka, “Interrogating emergent transport properties for molecular motor ensembles: A semi-analytical approach,” *PLoS Comput Biol*, vol. 12, no. 11, p. e1005152, 2016.
- [21] S. Talukdar, S. Bhaban, D. Materassi, and M. Salapaka, “Steady state dynamics of molecular motors reveals load dependent cooperativity,” in *Decision and Control (CDC), 2016 IEEE 55th Conference on*. IEEE, 2016, pp. 3356–3362.
- [22] S. Shastry and W. O. Hancock, “Neck linker length determines the degree of processivity in kinesin-1 and kinesin-2 motors,” *Current Biology*, vol. 20, no. 10, pp. 939–943, 2010.
- [23] K. Visscher and S. M. Block, “[38] versatile optical traps with feedback control,” *Methods in enzymology*, vol. 298, pp. 460–489, 1998.
- [24] M. J. Lang, C. L. Asbury, J. W. Shaevitz, and S. M. Block, “An automated two-dimensional optical force clamp for single molecule studies,” *Biophysical journal*, vol. 83, no. 1, pp. 491–501, 2002.
- [25] S. M. Block, “Kinesin motor mechanics: binding, stepping, tracking, gating, and limping,” *Biophysical journal*, vol. 92, no. 9, pp. 2986–2995, 2007.
- [26] T. Aggarwal, D. Materassi, R. Davison, T. Hays, and M. Salapaka, “Detection of steps in single molecule data,” *Cellular and molecular bioengineering*, vol. 5, no. 1, pp. 14–31, 2012.
- [27] C. Scherer, P. Gahinet, and M. Chilali, “Multiobjective output-feedback control via lmi optimization,” *IEEE Transactions on automatic control*, vol. 42, no. 7, pp. 896–911, 1997.
- [28] R. D. Vale, F. Malik, and D. Brown, “Directional instability of microtubule transport in the presence of kinesin and dynein, two opposite polarity motor proteins,” *The Journal of Cell Biology*, vol. 119, no. 6, pp. 1589–1596, 1992.
- [29] J. Gagliano, M. Walb, B. Blaker, J. C. Macosko, and G. Holzwarth, “Kinesin velocity increases with the number of motors pulling against viscoelastic drag,” *European biophysics journal*, vol. 39, no. 5, pp. 801–813, 2010.
- [30] S. Roychowdhury, S. Bhaban, S. Salapaka, and M. Salapaka, “Design of a constant force clamp and estimation of molecular motor motion using modern control approach,” in *American Control Conference (ACC)*, 2013. IEEE, 2013, pp. 1525–1530.
- [31] S. Roychowdhury, T. Aggarwal, S. Salapaka, and M. V. Salapaka, “High bandwidth optical force clamp for investigation of molecular motor motion,” *Applied Physics Letters*, vol. 103, no. 15, p. 153703, 2013.
- [32] T. Aggarwal, H. Sehgal, and M. Salapaka, “Robust control approach to force estimation in a constant position optical tweezers,” *Review of Scientific Instruments*, vol. 82, no. 11, p. 115108, 2011.
- [33] H. Sehgal, T. Aggarwal, and M. V. Salapaka, “Systems approach to identification of feedback enhanced optical tweezers,” in *NanoScience+Engineering*. International Society for Optics and Photonics, 2008, pp. 703 821–703 821.
- [34] M. Grant and S. Boyd, “CVX: Matlab software for disciplined convex programming, version 2.1,” <http://cvxr.com/cvx>, Mar. 2014.
- [35] J. J. Gorman, A. Balijepalli, and T. W. LeBrun, “Feedback control of optically trapped particles,” in *Feedback Control of MEMS to Atoms*. Springer, 2012, pp. 141–177.
- [36] K. Visscher, M. J. Schnitzer, and S. M. Block, “Single kinesin molecules studied with a molecular force clamp,” *Nature*, vol. 400, no. 6740, pp. 184–189, 1999.

## APPENDIX A KINESIN ASSAY

The kinesin bead motility assay is described in detail in [17]

## APPENDIX B FPGA IMPLEMENTATION

The  $2 \times 2$  controller  $K$  designed using the mixed objective  $H_2/H_\infty$  optimization approach consists of four transfer function  $K_{11}, K_{12}, K_{21}$  and  $K_{22}$ . The command signal  $u$  to the actuator, that regulates the load force on the bead at the reference value  $F_d$  is given by  $K_{11}F_d + K_{12}X_b$ , where  $X_b$  is the measured bead position. The estimated motor motion is obtained by  $\hat{X}_m = K_{21}F_d + K_{22}X_b$ . The transfer functions  $K_{ij}(s); i, j \in \{1, 2\}$  are obtained in the continuous form and have to be discretized in order to be implemented using FPGA hardware (National Instruments, *PCI7833R*). We utilize the bilinear transformation by substituting  $s = \frac{2}{T} \frac{z-1}{z+1}$  to obtain the equivalent discrete-time transfer functions  $K_{ij}(z); i, j \in \{1, 2\}$ , where  $T$  is the sampling period of the system (50 KHz in this article). The discrete transfer functions are implemented as infinite impulse response (IIR) filters using a direct form I architecture. For higher order filters, a direct form II architecture can also be utilized.

## APPENDIX C OPEN LOOP PLANT $P_{sys}$

The input output relationship of the open loop plant  $P_{sys}$  is given by,

$$[z \ y]^T = P_{sys}[w \ \tilde{u}]^T, \text{ where,}$$

$$P_{sys} = \begin{bmatrix} W_e & -W_e K_t K_m G & -W_e K_t G & W_e K_t A_c (1 - K_t G) & 0 \\ 0 & W_m & 0 & 0 & -W_m \\ 0 & 0 & 0 & 0 & W_\eta \\ 1 & 0 & 0 & 0 & 0 \\ 0 & G K_m & G & G K_t A_c & 0 \end{bmatrix}. \quad (5)$$

The state space dynamics of the open loop plant  $P_{sys}$  is given as,

$$\begin{aligned} \dot{x} &= Ax + B_w w + B \tilde{u}, \\ z &= C_z x + D_{zw} w + D_z \tilde{u}, \\ y &= Cx + D_w w. \end{aligned}$$

## APPENDIX D LMIS FOR MIXED $H_2 - H_\infty$ SYNTHESIS

A specific channel  $T_j$  is selected as

$$T_j(s) = L_j T(s) R_j$$

where,  $T(s)$  denotes the closed loop transfer function from  $w$  to  $z$ ,  $L_j$  and  $R_j$  select the appropriate input-output channels. The state space realization of  $T_j(s)$  is given as,

$$\left[ \begin{array}{c|c} \mathcal{A} & \mathcal{B}_j \\ \hline \mathcal{C}_j & \mathcal{D}_j \end{array} \right] = \left[ \begin{array}{cc|c} A + BD_K C & BC_K & B_j + BD_K F_j \\ B_K C & A_K & B_K F_j \\ \hline C_j + E_j D_K C & E_j C_K & D_j + E_j D_K F_j \end{array} \right],$$

where,  $B_j := B_w R_j$ ,  $C_j := L_j C_z$ ,  $D_j := L_j D_{zw} R_j$ ,  $E_j := L_j D_z$ ,  $F_j := D_w R_j$  and  $(A_K, B_K, C_K, D_K)$  denotes the state space realization of the controller  $K$ .

Optimization variables:  $\gamma, \hat{A}, \hat{B}, \hat{C}, \hat{D}, X, Y$ .

Objective function:  $\min \gamma$

Constraints:

LMIs for minimizing  $\|T_j\|_{H_\infty}$

$$\begin{bmatrix} AX + XA^T + \hat{B}\hat{C} + (\hat{B}\hat{C})^T & \hat{A}^T + (A + B\hat{D}\hat{C}) & * & * \\ \hat{A} + (A + B\hat{D}\hat{C})^T & A^T Y + Y A + \hat{B}\hat{C} + (\hat{B}\hat{C})^T & * & * \\ (B_j + B\hat{D}F_j)^T & (Y B_j + \hat{B}F_j)^T & -\gamma I & * \\ C_j X + E_j \hat{C} & C_j + E_j \hat{D}C & D_j + E_j \hat{D}F_j - \gamma I & \end{bmatrix} < 0, \quad (6)$$



LMIs for ensuring  $\|T_j\|_{H_2}^2 < \nu$

$$\begin{bmatrix} AX + XA^T + B\hat{C} + (B\hat{C})^T & \hat{A}^T + (A + B\hat{D}C) & B_j + B\hat{D}F_j \\ \hat{A} + (A + B\hat{D}C)^T & A^TY + YA + \hat{B}C + (\hat{B}C)^T & YB_j + \hat{B}F_j \\ (B_j + B\hat{D}F_j)^T & (YB_j + \hat{B}F_j)^T & I \end{bmatrix} < 0, \quad (7)$$

$$\begin{bmatrix} X & I & (C_jX + E_j\hat{C})^T \\ I & Y & -(C_j + E_j\hat{D}C)^T \\ C_jX + E_j\hat{C} & C_j + E_j\hat{D}C & Q \end{bmatrix} > 0, \quad (8)$$

$$Tr(Q) < \nu, \quad (9)$$

$$D_j + E_j\hat{D}F_j = 0, \quad (10)$$

Controller Reconstruction Steps:  
Determine the matrices  $M$  and  $N$  such that

$$MN^T = I - XY.$$

The controller is defined by

$$\begin{aligned} D_K &= \hat{D}, \\ C_K &= (\hat{C} - D_KCX)M^{-T}, \\ B_K &= N^{-1}(\hat{B} - YBD_K), \\ A_K &= N^{-1}(\hat{A} - NB_KCX - YBC_KM^T - Y(A + BD_KC)X)M^{-T}. \end{aligned}$$